Acta Materialia 284 (2025) 120631

Contents lists available at ScienceDirect

Acta Materialia

journal homepage: www.elsevier.com/locate/actamat

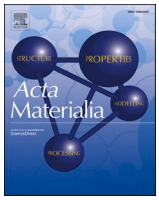

Full length article

Correlating aluminum layer deposition rates, Josephson junction microstructure, and superconducting qubits' performance

Jin-Su Oh [a], Cameron J. Kopas [b], Hilal Cansizoglu [b], Joshua Y. Mutus [b], Kameshwar Yadavalli [b], Tae-Hoon Kim [a], Matt Kramer [a], Alexander H. King [c], Lin Zhou [a,c,*]

[a] Ames National Laboratory, Ames, IA 50011, USA
[b] Rigetti Computing, Berkeley, CA 94710, USA
[c] Department of Materials Science and Engineering, Iowa State University, Ames, IA 50011, USA

ARTICLE INFO

Keywords:
Superconducting qubits
Josephson junction
Oxide tunnel barrier
Transmission electron microscopy
Grain boundary
Electron energy-loss spectroscopy
Coherence time

ABSTRACT

An ultra-thin aluminum oxide layer is a key component for Josephson junctions (JJ) in superconducting quantum bits (qubits). This layer serves as a barrier layer for Cooper pairs tunneling between the superconducting electrodes and significantly influences the overall performance of the junction. In this study, we investigate the impact of aluminum deposition rates on the microstructure and chemical variation of the aluminum oxide layer, as well as the device's yields and qubits' lifetimes. Surprisingly, although the oxide layer roughness and thickness variation improve noticeably with an increasing Al deposition rate from 0.5 Å/s to 5 Å/s, the qubit's coherence time is almost unchanged. We attribute this to the fact that Cooper pairs tunnel only through the thinnest region of the barrier. Additionally, we revealed a stress-induced grain boundary sliding short-circuit failure mechanism in the JJ. Our discovery provides a vital understanding of oxide microstructure and JJ functionality, which are critical for improving the coherence time of superconducting qubits.

1. Introduction

A superconducting transmon qubit with Josephson junctions (JJ), mostly comprising of Al/AlO_x/Al layers, has been a leading platform for gate-based quantum computing [1,2]. This system behaves as a non-linear inductive element in the electronic resonant circuits to realize superconducting artificial atoms [3–6]. Over the last two decades, rapid technical progress of a superconducting qubit in terms of relaxation time T_1 and coherence time T_2 has been achieved [7–9].

The performance of the transmon qubit is closely related to the structure of the Al/AlO_x/Al layers [10]. In particular, Cooper pairs tunnel through the ~2 nm thin AlO_x barrier layer in the JJ [11]. Previous results show that the tunneling current is inversely dependent on the thickness of AlO_x barriers. Zeng et al. [12] revealed that due to variations in the barrier thickness, only less than 10% of the total barrier volume is active for tunneling. This variation in the barrier thickness is also responsible for a larger effective conduction channel area and higher order tunneling process [13]. Moreover, Fritz et al. [14] have shown that the structural properties of the lower Al layer are responsible for the quality of the whole AlO_x barrier, which can be affected by deposition conditions [14–18].

The AlO_x barrier is typically fabricated by a diffusion-limited oxidation process of aluminum, which has many advantages, including reproducibility and uniformity for the large-scale process [19]. However, the diffusion process also produces an AlO_x layer with measurable densities of defects [20,21] that could host two-level systems (TLS) and become a major decoherence source in the transmon qubit [10,16,18,22–30]. These TLS defects can affect critical current fluctuations in the AlO_x-based junctions [31–33]. In addition, the complex microscopic structure of the disordered amorphous oxide barrier modifies charge dispersion and quasiparticle tunneling [34]. Thus, a comprehensive understanding of the electronic structures of Al and O across the AlO_x junction barrier and its relationship to film deposition conditions is critical for decoherence source elimination in future devices.

In addition, revealing the failure mechanism of the JJ is important

* Corresponding author at: Ames National Laboratory, Ames, IA 50011, USA.
E-mail address: linzhou@ameslab.gov (L. Zhou).

https://doi.org/10.1016/j.actamat.2024.120631
Received 2 February 2024; Received in revised form 23 August 2024; Accepted 5 December 2024
Available online 6 December 2024

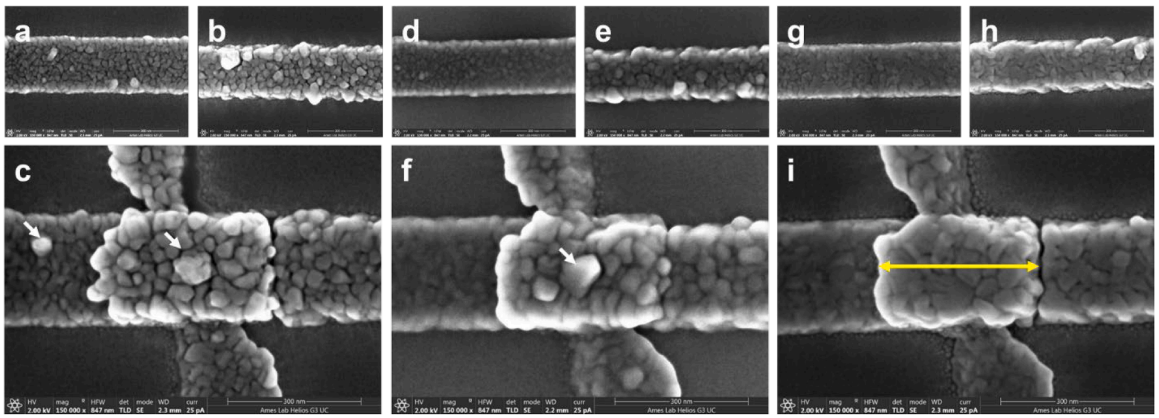

Fig. 1. SEM images of Josephson junctions from three different deposition rates. (a–c) A lower lead of JJ, an upper lead of JJ, and a JJ with Al deposited at a rate of 0.5 Å/s. (d–f) A lower lead of JJ, an upper lead of JJ, and a JJ with Al deposited at a rate of 2 Å/s. (g–i) A lower lead of JJ, an upper lead of JJ, and a JJ with Al deposited at a rate of 5 Å/s. As the deposition rate of Al increases, the grain sizes become larger with less large boulders, as indicated by white arrows. The grain sizes of upper leads are bigger than those of lower leads because of the Al layer thickness difference. The yellow double arrow indicates the width of JJ.

for enhancing the reliability of superconducting quantum devices. Up to now, failure studies on the tunnel junction were mainly based on electrical measurements in which the electrical field resulted in the dielectric breakdown of the barriers accompanied by microstructural evolution, including the formation of nanosized hillocks and voids [35–37]. For instance, Tolpygo et al. [38] proposed that the breakdown process occurs due to defect formation within the barrier caused by the applied electric field rather than from the junction fabrication process steps. On the other hand, Tyagi and Hinds [39] reported that a time-dependent stress relaxation could solely lead to tunnel junction failures. A recent study has demonstrated that the inherent disordered nature of the oxide barrier may be responsible for the formation of pinholes and weak-points in the junctions during the oxidation process [40]. However, the structural origin of the failure at the ultrathin tunnel barrier in the JJs without the application of a breakdown voltage is still unclear.

In this work, the microstructure of Al/AlO_x/Al layers in JJs are correlated with Al deposition conditions, failure rate, and room-temperature resistance and compared to qubit device performance. We reveal that the structure of the AlO_x film is closely related to the Al deposition rate. The spatial variation of the AlO_x layer is mainly related to the structure of the lower Al layer, including grain size, surface roughness, and crystal orientation. A clear electronic structure variation is observed across all AlO_x layers. However, the observed thickness variation and waviness of the AlO_x layer may not significantly impact qubit coherence times. In addition, we proposed a short-circuit failure mechanism of the Al/AlO_x/Al tunnel junction based on an observed unique microstructural feature. Our work points out the relevant factors that impact junction characteristics and defective states in the AlO_x layer and provides guidance for further device improvement by improving the quality of Al/AlO_x/Al barrier and metal layers.

2. Experimental

The qubit devices were fabricated on high-resistivity Si substrates with a Nb circuit layer and Al/AlO_x/Al Josephson junctions. The device wafers (that already have Nb circuitry) were coated with an e-beam resist and then patterned by e-beam lithography technique. Then, Al layers were deposited with a double angle electron beam evaporation system with a deposition rate of 0.5 Å/s, 2 Å/s, and 5 Å/s. Additional information about the fabrication process is available in Ref [41]. The film thicknesses of the lower Al layer and the upper Al layer are targeted at 30 nm and 50 nm, respectively. The base pressure of the deposition system prior to Al deposition was kept <5E-9 mbar. The lower Al layer (1st deposition) was oxidized in an integrated oxidation chamber prior to the top Al layer (2nd deposition) without breaking the vacuum in between depositions. Finally, excess metal was lifted off to from the Al/AlO_x/Al junctions on the wafer. Following JJ formation, we deposit a bandage using a similar lift-off process to connect the JJ metal to the Nb surface layer.

Qubit device dies are wire-bonded to a PCB, thermally anchored to the mixing chamber plate of a dilution refrigerator with base temperature $\leq$ 10 mK and shielded with superconducting and cryoperm magnetic shields. Input lines have a total of 76 dB of attenuation across many temperature stages, followed by a low-pass filter, while output lines are isolated with 4 circulators terminated to 50 Ω, and amplified with a HEMT followed by room-temperature amplifiers. Each test die has 14 flux-tunable qubits and 2 fixed qubits on two resonator feedlines without any qubit-qubit couplers. Coherence metrics are reported at f_{max} except for the flux spectroscopy measurements for TLS. We measure coherence times on each device in a continuous loop over several days (between ~60 and 300 measurements per qubit) and take the median of these measurements to avoid outliers. Strongly-coupled TLS are measured by performing qubit spectroscopy scans across the entire qubit tunability range, and fitting the coupling strength of any observed avoided crossings. This method can identify features with coupling strength larger than about g>0.5 MHz.

Secondary electron images for the JJ surfaces were acquired on SEM (Helios, Thermo Fisher Scientific Ltd.) at 2 kV under immersion mode with a through-lens detector, a probe current of 25 pA, and at a working distance of ~2 mm. TEM samples were prepared by a focused ion beam instrument with a gas injection system (Helios, Thermo Fisher Scientific Ltd.). The TEM samples were thinned to electron beam transparency by a Ga+ ion beam from 30 to 2 kV. The TEM samples were investigated by an aberration-corrected TEM (Titan Cube, Thermo Fisher Scientific Ltd.) at 200 kV. A high-angle annular dark-field (HAADF) detector was used for dark-field imaging in STEM mode with a convergent semi-angle and a collection semi-angle of 18 mrad and 74–200 mrad, respectively. Energy-dispersive X-ray spectroscopy (EDS) and electron energy-loss spectroscopy (EELS) studies were carried out with probe currents of 150 pA and 40 pA, respectively. Dual EELS was performed to acquire all-electron energy-loss (ELL) spectra. The plural scattering effect of all the raw ELL spectra was removed via Fourier-ratio deconvolution.

3. Results and discussion

3.1. AlO_x layer morphology and Al deposition rate

A higher Al deposition rate tends to create flatter Al film with a larger grain size. We studied JJs with Al deposition rates of 0.5 Å/s, 2 Å/s, and

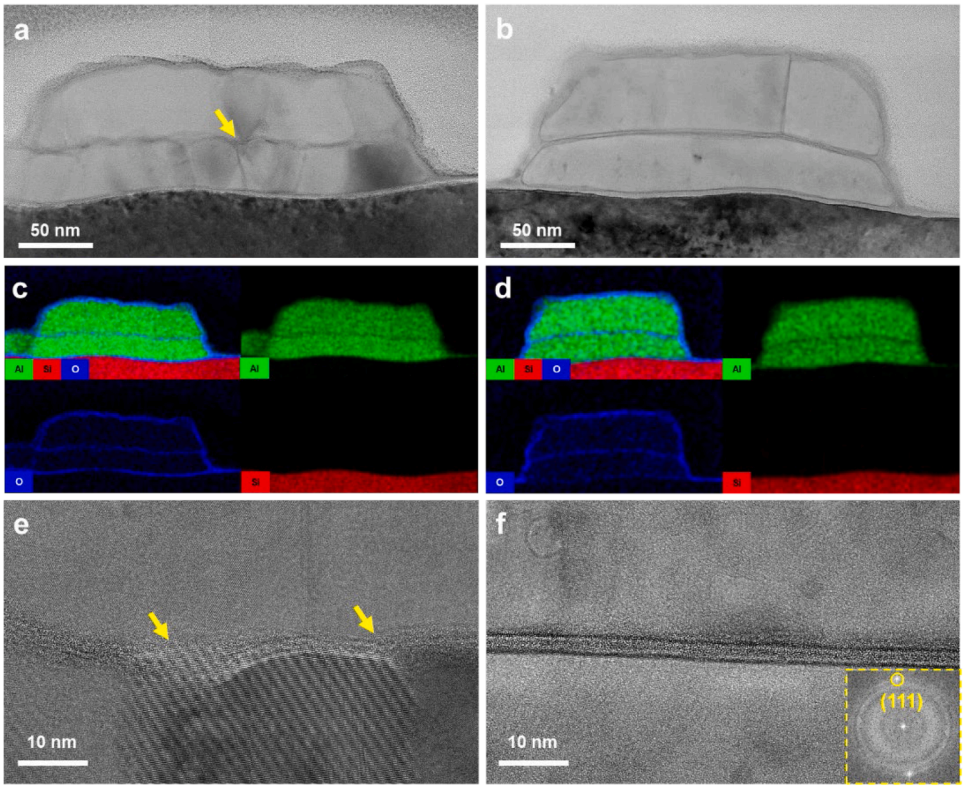

Fig. 2. Cross-sectional TEM images and EDS elemental distribution maps of JJ of superconducting transmon qubits with different Al deposition rates. (a, b) Low magnification images of JJ from different deposition rates of (a) – 2 Å/s, (b) – 5 Å/s. The yellow arrow denotes a grain boundary of the lower Al layer. (c, d) Corresponding elemental distribution maps of Al, O, Si. (e, f) High-resolution TEM images of the ultrathin oxide tunnel barriers for Al deposition rates of (e) – 2 Å/s, (f) – 5 Å/s. (e) Grain boundaries of the lower Al layer are indicated by yellow arrows. Grain boundary grooving is clearly observed, leading to an increased AlO_x layer thickness. (f) The AlO_x layer is flatter and has a more uniform thickness. Inset: Fast-Fourier transformed micrograph from the lower Al grain.

5 Å/s. The targeted film thicknesses of the lower and upper Al layers are 30 nm and 50 nm, respectively. SEM images show the surface details of JJs and their upper and lower leads (Fig. 1). For samples with the same deposition rate, the grain size of the upper layer is typically larger than that of the lower layer because thicker film promotes grain boundary movement during deposition and results in increasing lateral grain size [42]. For samples with different Al deposition rates, a higher deposition rate tends to increase grain size and reduce surface roughness. In addition, with an increased deposition rate, the density of the large boulders (as indicated by white arrows in Fig. 1) tends to decrease. This trend could be explained in terms of Al-adatom. A higher deposition rate suppresses the mobility of Al-adatom. Thus, at the initial coalescence stage, smaller islands form to make continuous films. Consequently, the total grain boundary energy of the film becomes higher, leading to a higher driving force for larger grains. In addition, grain coarsening increases the number of grains with a preferred orientation toward the lowest surface energy [43]. This preferred orientation also suppresses hillock formation [44]. Therefore, the homogeneity of the grain orientation flattens the film surface [14]. Furthermore, a higher Al deposition rate impedes the surface mobility of adatoms near the grain boundaries, leading to fewer boundary grooves [42].

The surface roughness of the lower Al layer determines the AlO_x layer thickness uniformity. Fig. 2 compares the cross-sectional microstructure of JJs with different Al deposition rates. Bright-field TEM micrographs (Fig. 2a, b) show larger Al grain size in JJs with a higher deposition rate, consistent with SEM results in Fig. 1. An example of a grain boundary in the lower Al layer deposited at the rate of 2 Å/s is denoted by a yellow arrow in Fig. 2a. Interestingly, the lower Al layer of the JJ deposited at the rate of 5 Å/s has a grain with a lateral size of ~ 240 nm (Fig. 2b), which is ~8 times the film thickness. Grain coarsening during deposition generally leads to lateral grain sizes of up to ~4 times the film thickness [45], which is called normal growth. However, at a high deposition rate, the driving force for coarsening is large enough for huge grain growth [14,46], called abnormal grain growth [47]. Those grains generally grow along the [111] crystallographic direction to minimize surface energy [43]. High-resolution TEM images of the AlO_x layers with different deposition rates are shown in Fig. 2e, f, with grain boundaries indicated by yellow arrows. It is obvious that the existence of grain boundaries in the lower Al layer of the JJ not only impacts waviness but also the thickness of the AlO_x tunnel barrier. A thickness increase of the AlO_x layer at the grain boundary caused by boundary grooving is observed (Fig. 2e), which may be related to faster oxygen diffusion along the grain boundary triple junctions [15]. In contrast, the AlO_x layer grown on the lower Al layer with a deposition rate of 5 Å/s exhibits flatter morphology and more uniform thickness (Fig. 2f). A preferred growth along the [111] direction is observed from the fast Fourier transformed micrograph of the lower Al grain, as shown in the inset of Fig. 2f.

3.2. *Electronic structural variation across the AlO_x layer*

We observed a gradual change of bonding states across the thin AlO_x barriers. Energy-loss near edge structure (ELNES) analysis (Fig. 3) was carried out across the AlO_x layer in the Al L_{23} edge energy region, which corresponds to the excitation of a 2p electron to unoccupied s- and d-like density of states [48]. We performed spatially resolved EELS linescan at the atomic scale to investigate the homogeneity of the AlO_x barrier in terms of electronic structure. Colored spots in the HAADF-STEM micrograph in Fig. 3a indicate positions from which EEL spectra are obtained. Two main peaks close to 77 eV and 80 eV of the Al L_{23} edge (labeled as A and B, respectively, in Fig. 3b) are commonly observed in amorphous AlO_x [17,18,49]. The A and B peak positions vary with

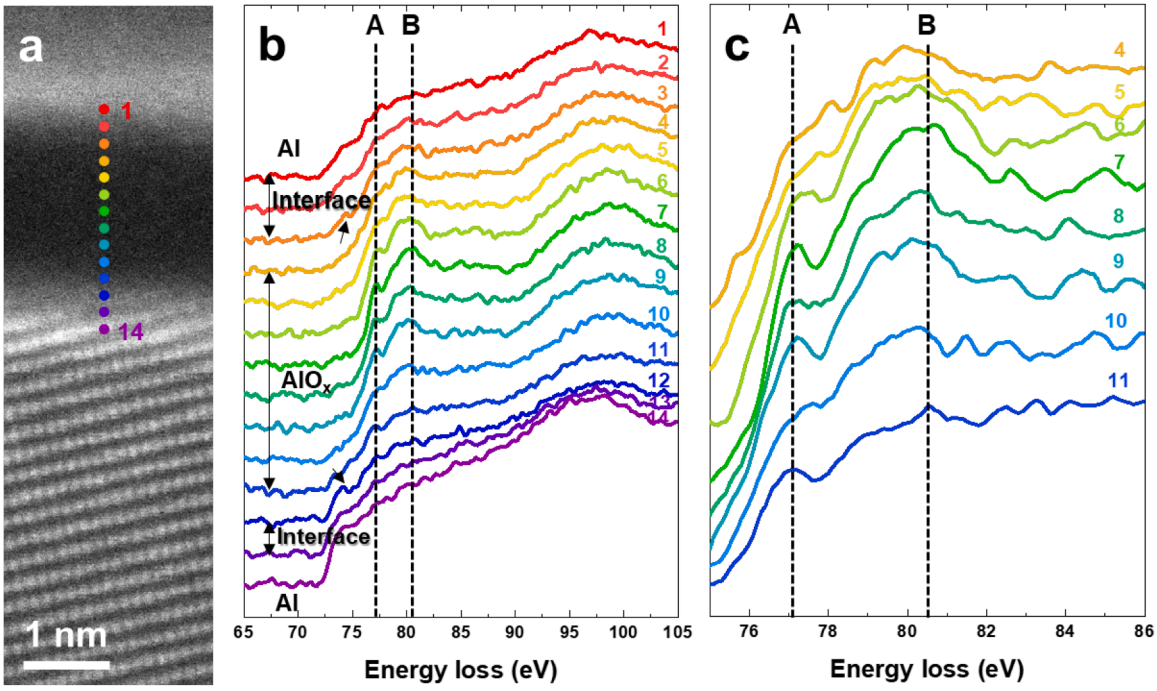

Fig. 3. EELS line profile across $Al/AlO_x/Al$ layers showing gradual changes in electronic structures of Al. (a) HAADF-STEM micrograph. Colored spots denote the positions in which EEL spectra are acquired. (b) Spatially resolved EEL spectra showing ELNESs of Al L_{23} edge. Two peaks (A and B) are well separated. The probed positions are divided into Al electrodes, overlapping interfaces, and pure amorphous AlO_x region by black double arrows. Black arrows indicating peaks at 74 eV from lines 3 and 12 attest to overlaps between Al and AlO_x along the electron beam direction. (c) Magnified EEL spectra from line 4 to line 11. A positive shift (higher energy) of the peak A position as the examined position approaches the upper Al/AlO_x interface is clearly shown. This JJ was fabricated at the Al deposition rate of 2 Å/s.

changes in coordination numbers and bonding characteristics of Al. Kimoto et al. [50] interpreted the A and B peaks to tetrahedrally and octahedrally coordinated Al in AlO_x, respectively. His assignment has been predominantly applied to explain ELNESs of Al fabricated under various conditions [16–18]. Nevertheless, perceiving this tetrahedral and octahedral coordination assignment is not universally applicable for various coordinated Al, as deviations from this assignment have been observed [48,49]. More generally, as the coordination number of Al increases, peak A is observed to move towards higher energy levels, a phenomenon that has been clearly established in other literature [48]. In our sample, the Al ELNESs of AlO_x are observed from spots 4 to 11. Spots 3 and 12 show additional peaks at 74 eV, which are from Al metal due to the overlap of Al and AlO_x along the electron beam direction at the interface. The right shift of peak A positions in AlO_x layer towards the upper-Al/AlO_x interface is observed (Fig. 3c), indicating an increase of Al coordination number and oxygen content [18,48,49,51]. This nonuniformity of chemistry perhaps originates from the well-known self-limiting oxidation process, which induces a gradient of oxygen

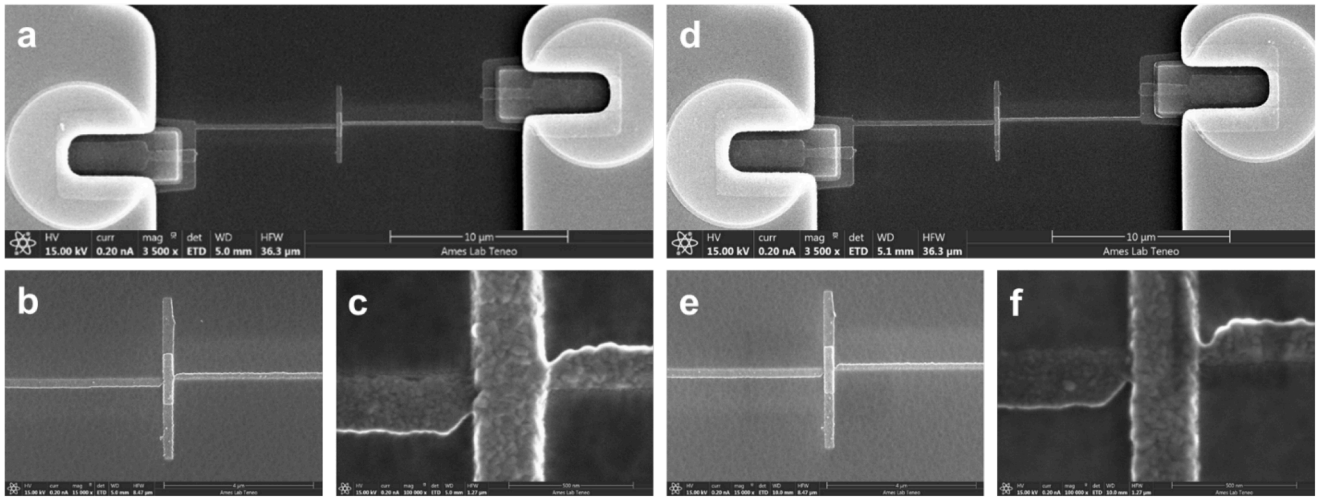

Fig. 4. SEM images of the short-failed and the normal qubits. (a) A low magnification SEM image of the short-failed qubit including lower and upper Al leads, a JJ, and Band-Aid regions. (b-c) Low and high magnification SEM images of the lower and upper Al leads and the JJ of the short-failed qubit. (d) A low magnification SEM image of the normal qubit including lower and upper Al leads, a JJ, and Band-Aid regions. (e-f) Low and high magnification SEM images of the lower and upper Al leads and the JJ of the normal qubit. No difference in microstructural surface features is observed between the short-failed and normal qubits. These JJs were fabricated at the Al deposition rate of 2 Å/s.

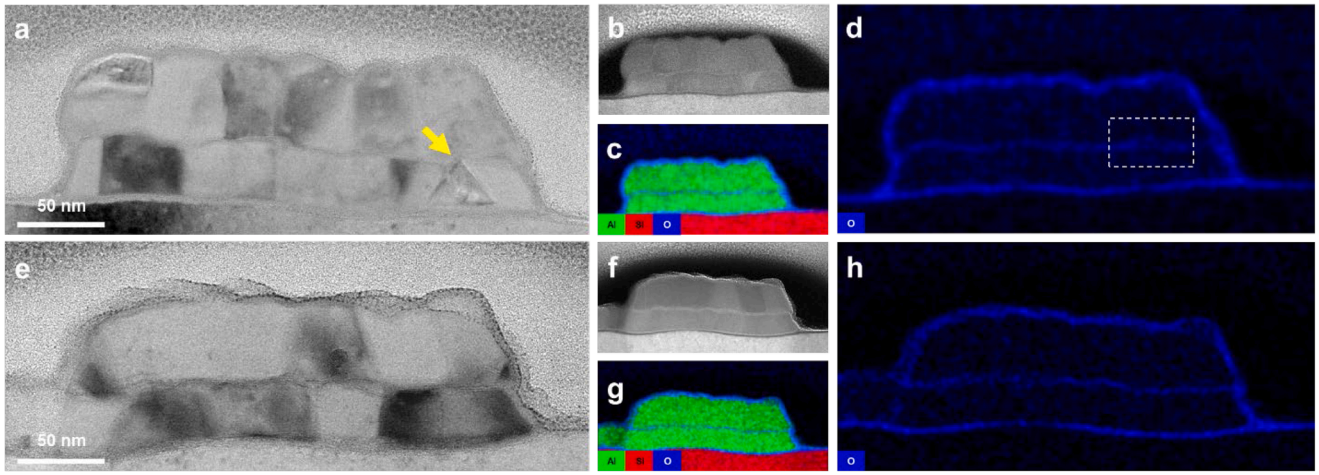

Fig. 5. Cross-sectional TEM comparison between the short-failed and the normal JJ. (a) An overall microstructure of the short-failed JJ. A sharp triangular feature of the grain structure of the lower Al layer in the short-failed JJ is denoted by the yellow arrow. (b–d) Corresponding HAADF-STEM micrograph, color mixed EDS elemental distribution map, and oxygen distribution map. A white dashed box shows the blurred AlO_x barrier feature. (e) An overall microstructure of the normal JJ. (f–h) Corresponding HAADF-STEM micrograph, color mixed EDS elemental distribution map, and oxygen distribution map. These JJs were fabricated at the Al deposition rate of 2 Å/s.

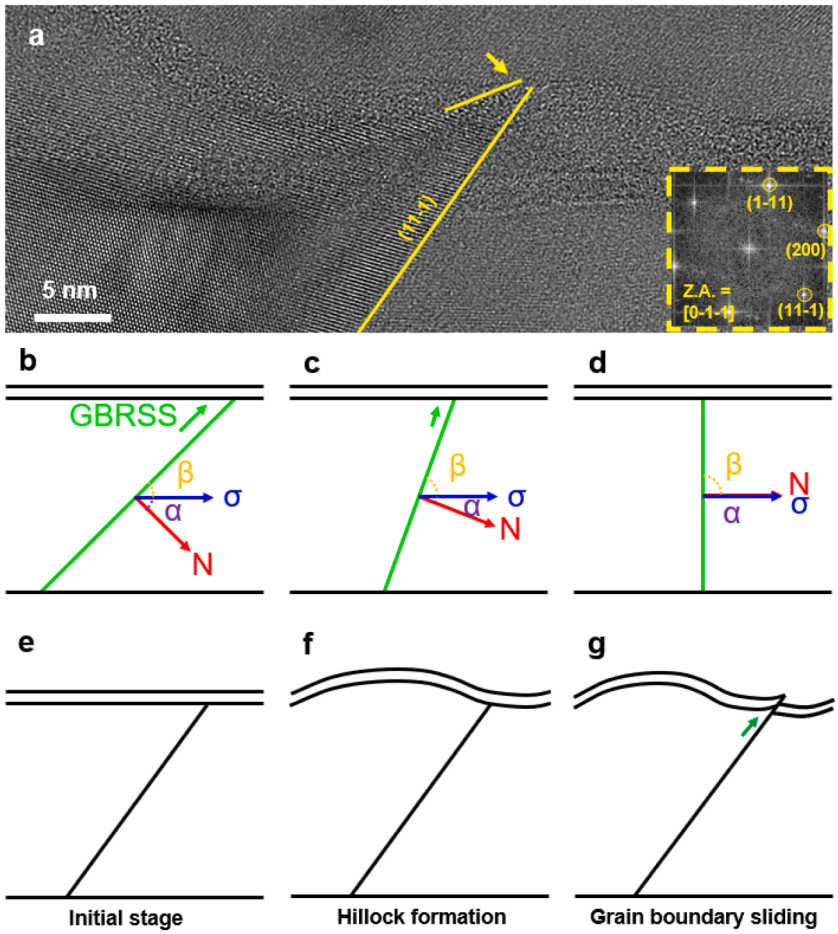

Fig. 6. Microscopic origin of short-circuit failure in JJ. (a) High-resolution micrograph of the region of interest showing a sharp edge of the grain boundary denoted by a yellow arrow, where short-circuit failure may occur by breaking the AlO_x barrier. Inset: reduced fast Fourier transformed micrograph from the lower left-hand grain in (a). (b–d) Schematic showing grain boundary resolved shear stress on the grain boundary and its dependence on the grain boundary angle to the substrate normal. σ is compressive stress applied to the left grain, N is the boundary plane normal, α is the angle between the boundary plane normal and applied stress, and β is the angle between the boundary plane tangent and applied stress. Light green arrows indicate the magnitude and direction of the grain boundary resolved shear stress. (e–g) Schematic representing short-circuit failure mechanism in $Al/AlO_x/Al$ based JJs. (e) An inclined straight grain boundary on the initial stage. (f) Compressive stress relaxation leads to hillock formation. (g) Resolved shear stress acting on the grain boundary results in sliding. The green arrow indicates the sharp-tip shape of the grain where the short-circuit failure occurred.

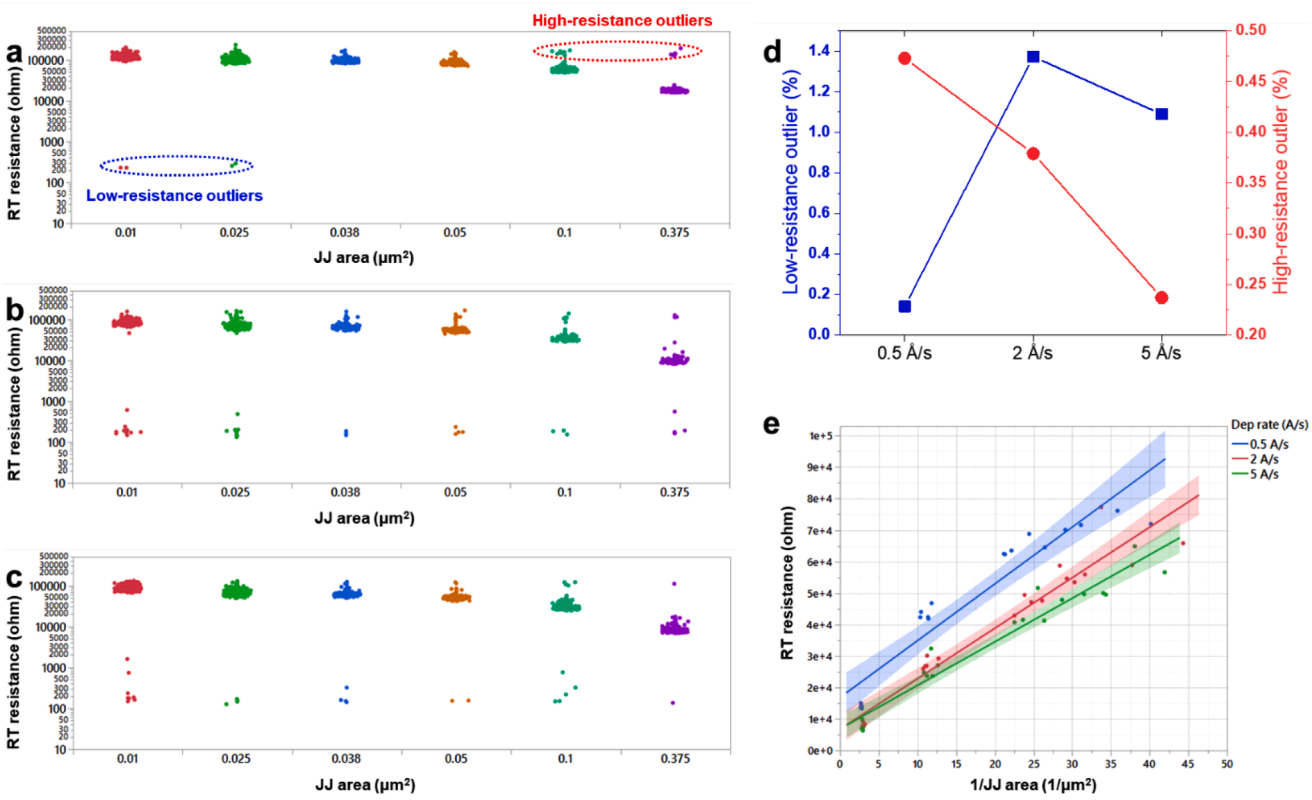

Fig. 7. Room-temperature resistance measurements of JJ at three different deposition rates and failure rates as a function of deposition rate. Resistances are plotted as a function of junction area, fabricated by different Al deposition rates of (a) 0.5 Å/s, (b) 2 Å/s, and (c) 5 Å/s. Low resistance outliers ("short-circuit") are visible below the main groupings, and high resistance outliers ("opens") are visible above the main groupings. (d) The failure rates (short-circuit; blue squares, opens; red circles) vs deposition rate plot. (e) RT resistance (ohm) vs 1/JJ area ($1/\mu m^2$) plot showing a trend of higher resistances with lower deposition rate and lower resistances with higher deposition rate across various JJ sizes. The solid lines are linear lines of best fit, while the shaded area is uncertainty around the fit line.

concentrations within the AlO_x layer [52]. Because the average number of bonds between Al and O can affect the AlO_x tunnel barrier resistivity [18], these gradual changes in chemical features can also impact the charge carrier tunneling. For instance, this stoichiometric gradient may result in current hot spots at the edges of the barrier [40]. In addition, electronic states related to the lower Al coordination number near the lower Al/AlO_x interface are associated with the vacancy density, which in turn can act as energy dissipation traps, leading to subgap leakage of the JJs [16,53]. The above result confirms the chemical inhomogeneity is present in the ultrathin AlO_x barriers, introducing structural defects and causing device decoherence. Our recent report proposed a new method to mitigate this inherent inhomogeneity nature of the AlO_x barrier, called alternating bias-assisted annealing (ABAA), that leads to an overall higher junction resistance and higher coherence time [54]. We observed that the ABAA-treated JJs exhibited a higher coordination number of Al within the barriers, accompanied by a more homogeneous electronic state compared to the untreated JJs. We attribute the enhanced coherence of the ABAA-treated JJs to this observation [54].

3.3. Short-circuit failure mechanism

Residual stress from fabrication procedures may cause plastic deformation of some Al layers inside the JJ, resulting in short-circuit device failure. No abnormal microstructural feature that is responsible for or originates from the short-circuit failure is observed when examining the surface from SEM images of JJ in a short-circuit failed (short-failed) qubit (Fig. 4a–c) and a qubit with expected resistance (normal) (Fig. 4d–f), both of which were fabricated with a deposition rate of 2 Å/s. For this investigation, we will refer to a short-circuit failed qubit as a "short-failed" qubit, and a qubit with expected resistance as a "normal" qubit. The measured resistances of the short-failed and normal JJs are 208 Ω and 11,571 Ω, respectively. We subsequently examined cross-sectional TEM images of a short-failed JJ (Fig. 5a–d) and a normal JJ (Fig. 5e–h). A triangular shape grain was observed in the short-failed JJ, as indicated by a yellow arrow in Fig. 5a. The corresponding EDS oxygen map shows a blurred distribution of oxygen at the tip of the triangle (Fig. 5d). A sharp tip at the top right-hand side of the triangular grain boundary broke the continuous AlO_x layer, as indicated by a yellow arrow in the high-resolution cross-sectional TEM image in Fig. 6a. Fast Fourier transformed micrograph from the bottom left-hand side grain is shown in the inset of Fig. 6a.

The observed short-circuit failure may originate from the plastic deformation of the triangular Al grain, caused by stress relaxation in the thin film. Intrinsic and thermal stress are the two main types of residual stress in thin films. Intrinsic stress is built during the growth stage from in-grown defects or structural mismatch [55] in thin films. In many cases, intrinsic stress eventually becomes compressive, particularly in face-centered-cubic metals with low melting temperatures [56,57]. The residual compressive stress can relax with time, causing the formation of nanohillocks [39], which lead to the waviness of the amorphous AlO_x layer and create weak points or microcracks in the AlO_x layer [58]. On the other hand, thermal stress results from a large difference in thermal expansion coefficient between the lower Al thin film (23.1×10^{-6} K^{-1}) and the Si (2.6×10^{-6} K^{-1}) substrate during thin film deposition [55]. This thermal stress produced in the films can be estimated using a simple equation [59],

$$\sigma = E \cdot \Delta\alpha \cdot \Delta T \quad (1)$$

where E is an appropriate biaxial modulus, $\Delta\alpha$ is the difference in linear expansion coefficients between the film and the substrate, and ΔT is the

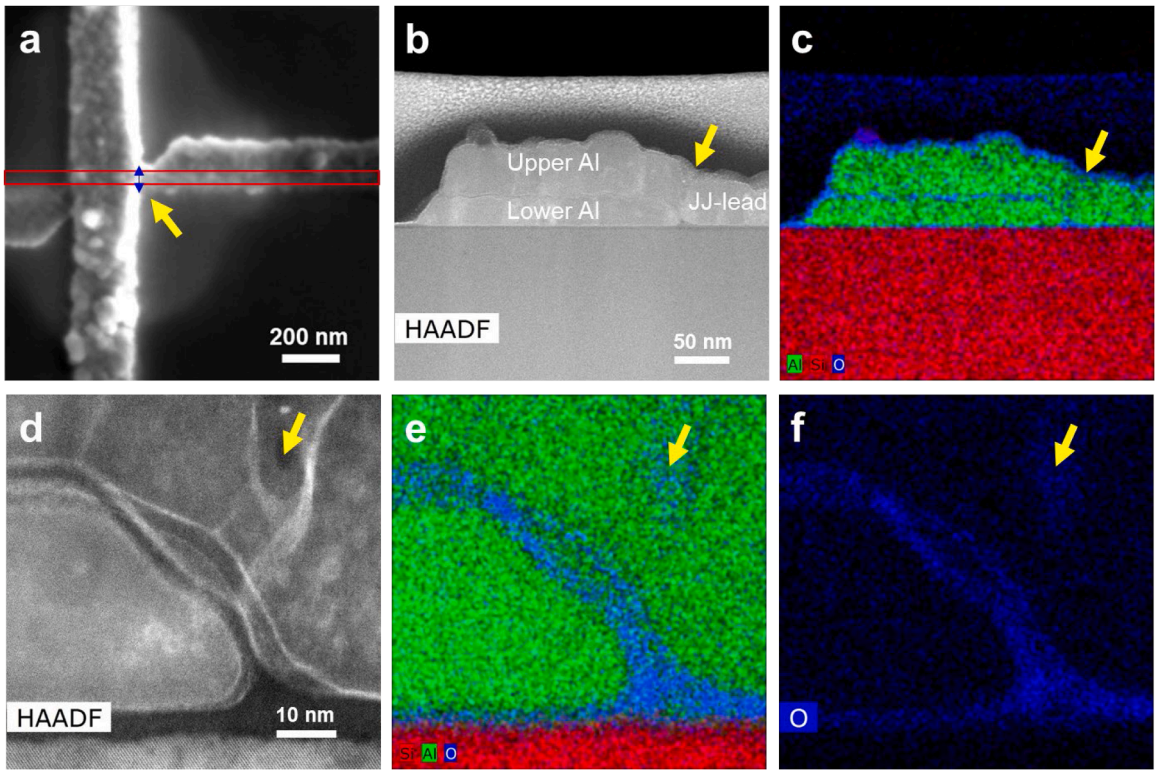

Fig. 8. Notch structure in upper Al layer of JJ. (a) SEM image of JJ from which FIB lamella is fabricated, as indicated by the red box. Irrespective of the JJ's width, the width of the contact area between the upper Al electrode and the JJ-lead remains constant, as indicated by the blue double arrow. (b) HAADF-STEM image and (c) corresponding Al, Si, and O EDS elemental map of JJ. (d) high-magnification HAADF-STEM image and (e) corresponding Al, Si, O EDS elemental map, and (f) O EDS elemental map of JJ at the interface between the upper Al electrode and the upper JJ-lead. Yellow arrows indicate a notch position, where noticeable oxygen concentration is observed. The JJ was fabricated at an Al deposition rate of 2 Å/s.

temperature change [59]. Our fabrication process includes thermal processing steps up to 180 °C, producing estimated thermal stress over ~200 MPa.

The deformation mechanism of a metal is generally related to its grain size. The deformation mechanism switches from dislocation activities to grain boundary sliding (GBS) for nanostructured metals with grain size below a critical value [60,61]. As the grain size where the deformation occurred in the sample is ~30 nm, which is below the critical grain size of Al (~110 nm) [62], GBS tends to be the dominant deformation mechanism in the lower Al layer. The grain boundary resolved shear stress (GBRSS), a component of the applied stress on the boundary plane, determines whether to trigger the GBS [63,64]. Similar to the Schmid factor in slip planes [65], the GBRSS can be estimated by,

$$GBRSS = \sigma \cos\alpha \cos\beta \quad (2)$$

where σ is applied stress, α is the angle between the boundary plane normal and applied stress, and β is the angle between the boundary plane tangent and applied stress [65], as schematically illustrated in Figs. 6b-d. Under a fixed applied stress σ, The GBRSS reaches its maximum value when both α and β are 45° (Fig. 5b). The GBRSS decreases to zero as α and β go to 0° and 90° (Fig. 6d). The grain boundary that caused the observed failure in the sample is a (111) type grain boundary, as observed in Fig. 6a. GBS occurs along the direction of maximum GBRSS where β is minimized. Thus, the direction of GBS should be in the same plane as the one comprised of the boundary plane normal and the applied stress. Consequently, this indicates, in turn, that $\alpha + \beta$ should be equal to 90°. Then, the GBRSS is expressed as,

$$GBRSS = \sigma \cos\alpha \cos(90^\circ - \alpha) = \frac{1}{2}\sigma \sin\sin 2\alpha \quad (3)$$

Given the measured angle of α is ~40°, the GBRSS was highly likely to be higher than the critical shear stress for Al with the grain size of ~30 nm (~70–100 MPa) [66]. In addition to GBRSS, it is worth noting that the grain boundary, which experienced the GBS, is a straight (111) boundary with the lowest boundary energy in nanocrystalline aluminum thin film [67], as indicated by a yellow line in Fig. 6a. This straight feature of the boundary plane is another important factor for GBS. Venkataraman et al. [68] showed that grain boundaries with large curvature do not experience the GBS even though the GBRSS is large enough for sliding, concluding that not only GBRSS but also the grain boundary straightness was a key parameter in determining GBS propensity [68,69]. GBS lead to the formation of a sharp tip that broke the continuous AlO_x layer (Fig. 6a). Schematics representing the observed short-circuit failure of the Al/AlO_x/Al JJs are shown in Fig. 6e–g.

3.4. AlO_x structure, JJ failure rate, and qubit performance

The deposition rate has an obvious impact on the yield of the transmon qubits. Fig. 7a-c shows the measured room-temperature resistance of different JJ areas at different Al deposition rates. As the area of the JJ increases, the average resistance of the junction decreases, attributed to the increase in the barrier area. Two types of failures are observed; low-resistance outlier (also called short-circuit failure) and high-resistance outlier (measured resistance is way higher than targeted resistance), as plotted in Fig. 7d. We see the lowest short-circuit failure rate (0.14%) in 0.5 Å/s deposited JJs, and the rate increases to 1.37% and 1.09% in 2 Å/s and 5 Å/s deposited films, respectively. It has been reported that a short-circuit failure of ultrathin tunnel barriers (without applying a breakdown voltage) mainly occurs by the formation of hillocks through mechanical compressive stress relaxation [39]. Also, it is well known that the formation of nano-hillocks is more likely to occur in non-(111) oriented grains [44]. However, our results show that with a

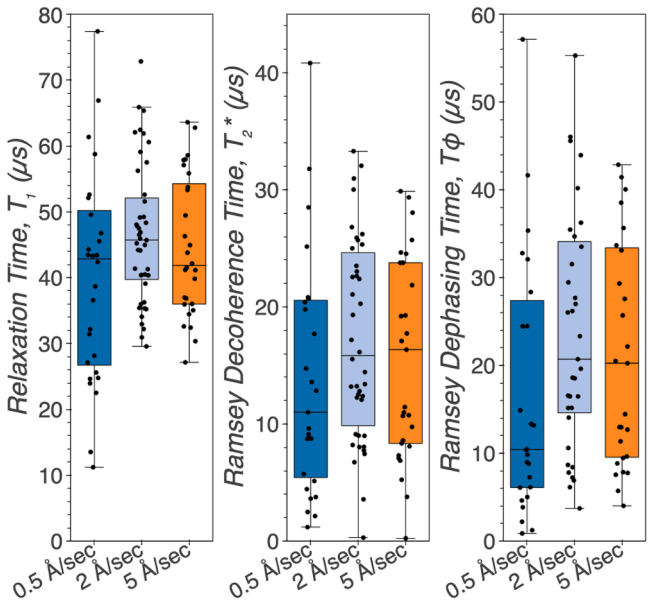

Fig. 9. Comparison in relaxation time (T_1), Ramsey decoherence time (T_2*), and Ramsey dephasing time (T_ϕ) of three sets of qubits fabricated with Al deposition rates of 0.5, 2, and 5 Å/s. Each data point represents a median characteristic for a single qubit where $n = 28$ for 0.5 and 5 Å/s, and $n = 43$ for 2 Å/s.

higher deposition rate, the grains tend to orient along the [111] direction with less hillock formation (as shown in Fig. 1) but with higher failure rates. Thus, compressive stress induced hillock formation is not the predominant failure mechanism for the short-circuit in these JJs. Instead, other failure mechanisms, such as GBS at the lower Al electrode are more likely to be responsible for the short-circuit, as discussed in Section 3.3. Moreover, high-index grain boundary planes tend to transfer to low-index grain boundary planes as the deposition rate increases [14]. Since the preferred growth direction is close to the [111] crystallographic orientation at a higher deposition rate, the probability of forming low energy (111) grain boundaries [67] inclined to the substrate normal also increases (Figs. 6b-c). In this geometric condition, the applied compressive stress is larger and triggers GBS more easily. Thus, we observe higher short-circuit failure rates at higher Al deposition rates (2 Å/s and 5 Å/s). On the other hand, as the grain size increases with the deposition rate, the lower Al film's total grain boundary density decreases, which reduces the number of boundaries experiencing GBS, resulting in a slight decrease in the failure rate at 5 Å/s compared to at 2 Å/s.

In contrast to the short-circuit failure rate, the high-resistance failure rate ("open-circuit") gradually improves with higher deposition rate, decreasing from 0.47% to 0.24% as the deposition rate increases from 0.5 Å/s to 5 Å/s (Fig. 7d). As discussed earlier in Section 3.1, an uneven distribution of the AlO_x barrier layer's thickness could lead to a reduced active area in the total barrier volume. This reduction in the active area results in increasing resistance of JJs at lower deposition rates. Fig. 7e shows the Resistance (ohm) vs. 1/JJ area ($1/\mu m^2$) plot, where the JJ area was calculated from SEM images of individual JJs. This type of plot removes the effect of JJ size on resistances and enables comparison of the Resistance-Area product, which shows the effect of the oxide barrier on the resistances. As seen in Fig. 7e, JJ resistances get higher with a low deposition rate for the same size JJs, indicating the uniform active area of the oxide barrier getting smaller due to the increased grain boundaries with a lower deposition rate. The relatively thicker oxide at the grain boundary (grain boundary grooving) can cause a reduction in the uniformity of the oxide layer. Moverover, our TEM study showed a notch between the upper Al layer and the upper JJ-lead, as shown in Fig. 8 (indicated by yellow arrows). The notch is likely formed due to the non-uniform formation of the upper Al layer at the intersection with the lower Al electrode sidewall (at the "climb-over") [70]. This notch contains a considerable amount of oxygen between the upper Al electrode and the upper JJ-lead, as shown in Fig. 8f, which may be responsible for the high-resistance outliers. A lower deposition rate results in a less uniform coverage that may increase the size of the notch and the possibility of high-resistance outliers (failure) formation.

Table 1
Failure rates (short and open), average number of strongly-coupled TLS ($g > 0.5$ MHz), and coherence times (T_1, T_2*, and T_ϕ) of JJ and qubits fabricated from three different Al deposition rates. The total tunability range for each deposition rate is between 9 and 10.6 GHz.

Dep rates	Failure rates (%)		Average # of TLS (TLS/GHz)	Coherence times (μs)		
	Short	Open		T_1	T_2*	T_ϕ
0.5 Å/s	0.14	0.47	1.3	43 ±20	11 ±14	10 ±21
2 Å/s	1.37	0.38	0.6	46 ±11	16 ±10	21 ±20
5 Å/s	1.09	0.24	0.9	42 ±11	16 ±12	20 ±23

The correlation between the Al deposition rate and qubit coherence, as shown in Fig. 9, appears to be weak. Median T_1 values for each Al deposition rate are T_1 (0.5 Å/sec) ≈ 43±20 μs, T_1 (2 Å/sec) ≈ 46±11 μs, and T_1 (5 Å/sec) ≈ 42±11 μs, where the uncertainties are the standard deviations. The similarity between all sets in T_1, as well as the T_2* and T_ϕ suggest that, although smaller grains introduce larger oxide thickness variation due to grain boundary grooving, the thicker oxides around the grain boundary region do not significantly affect dissipation and decoherence in the tunnel barrier, or that loss at other interfaces dominates.

In contrast to the coherence metrics, qubit spectroscopy measurements for the three different sets do show that the number of strongly-coupled TLS depend on Al deposition rate. Over a number of tunable qubits with varying tunable ranges, we report TLS as the number of strongly-coupled avoided crossings over the sum of the tunable range (Table 1). In the low deposition rate (0.5 Å/*sec*) group we find 12 TLS over 9.1 GHz in 20 qubits ≈ 1.3 TLS/GHz; for the middle deposition rate (2 Å/*sec*) there are 6 TLS over 10.6 GHz in 27 qubits ≈ 0.6 TLS/GHz; and for the high deposition rate (5 Å/*sec*) there were 9 TLS over 9.6 GHz in 23 qubits ≈ 0.9 TLS/GHz. The majority (80%) of all observed TLS in this study exhibit a coupling strength $g \leq 1$ MHz, where $g \approx 0.5$ MHz is the detection limit. Although the sample set is small, these results show that the middle, 2 Å/*sec*, deposition rate has the fewest TLS. This shows that there is some dependence in TLS on Al deposition rate, but competing mechanisms may be at play, and it is necessary to optimize processing to find a TLS minimum. The relationship between possible TLS density in JJ and Al deposition rate can be complex, depending on the process parameters and substrate conditions. A positive aspect of a higher Al deposition rate in reducing the density of TLS defects might be less thickness fluctuation in the AlO_x barrier at a higher deposition rate. The variation in barrier thickness may create weak points, influencing higher-order tunneling and charge dispersion of qubits [13,34]. Also, as the preferred growth of (111) crystal plane at a higher deposition rate tends to exhibit more spatially uniform transport properties across the junction, the reduced variance in the current density through the junction could result in reduced coupling to TLS defects [40]. Furthermore, thickness variation in the AlO_x barrier may affect the electronic state variation inside because thicker AlO_x may generate more defective structures near the lower interfaces between AlO_x and Al. The non-uniformity of electronic structure is directly related to atomic structural defects in the AlO_x tunnel barrier, which are believed to be a major TLS source of superconducting qubits [23]. In addition, enhanced oxygen diffusion into the grain boundaries [71] of the lower Al during the oxidation process could be a possible TLS source [22]. As such, aluminum film with smaller grain tends to have a higher grain boundary

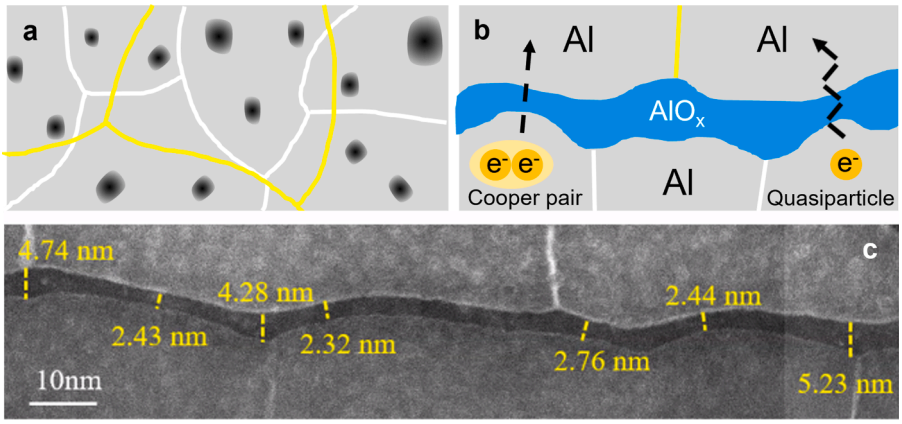

Fig. 10. Schematic diagram of the microstructure of a JJ. (a) Top (plan) view. The yellow line and white line indicate grain boundaries of the upper and lower Al layers, respectively. (b) Cross-sectional view. The irregular thickness of the AlO_x barrier leads to a reduction in the area that is responsible for tunneling. The black gradient irregular circles in (a) and the black dashed arrows in (b) depict preferential carrier tunneling channels. (c) High-resolution cross-sectional HAADF-STEM image explicitly shows irregular spatial variation of the AlO_x barrier in thickness.

volume fraction, thus with a high amount of potential decoherence source. On the other hand, the deposition rate itself is an important factor that can influence the quality of the Al thin film, including defect density. A higher deposition rate may result in a higher defect density due to insufficient time for atoms to reach their energetically preferred sites on the substrate. These defects can manifest in the form of point defects, lattice mismatches, and other forms of structural non-uniformity, leading to imperfect crystalline structures, which in turn can introduce uncontrolled variability into the qubit operation. On the contrary, a slower deposition rate can allow for more atomistic surface mobility, giving atoms the necessary time to find their optimal position before being overlaid by subsequent layers of deposition material. This can lead to higher quality films with lower defect densities although this does not mean that a slower deposition rate always results in low defect densities. Therefore, it's a balance between the AlO_x layer and Al superconductor, and the optimized Al deposition rate. For our tool and conditions, it is may be near 2 Å/s for the fewest strongly-coupled TLS. The summary of yields, average number of TLS, and coherence times of transmon qubits with different Al deposition rates are shown in Table 1.

We can model this phenomenon using a schematic diagram illustrating the microstructure of a JJ, as depicted in Fig. 10. Generally, grain boundaries of superconducting films may act as a weak JJ [72], which is also characterized by residual resistance ratio [73,74]. Therefore, as the electric field in 2-D circuit is parallel to a chip plane, the larger grain size of Nb thin films tends to exhibit a higher coherence time in superconducting qubits [73] or a higher internal quality factor in superconducting coplanar waveguide resonators [74]. In contrast, in the $Al/AlO_x/Al$ junction, the electric field and grain boundary planes are nearly parallel, leading to vertical Cooper pair and quasiparticle tunneling (Fig. 10b). Along the electric field direction, the thinnest barrier area (less than 10% of the total barrier volume) that is active for quasiparticle tunneling [12], does not tend to form at the grain boundary region due to the grain boundary grooving (Fig. 10c). Consequently, grain boundary related loss in Al layers (as weak JJs) is less prominent than that in Nb capacitor pads in transmon qubits or coplanar waveguide resonators [74]. Therefore, improving JJ microstructure may focus on creating textured columnar Al grains. This would allow the thinnest Al-oxide layer to form from lattice planes with the same crystal orientation in the Al film. This approach could lead to more microstructurally and chemically uniform structures, potentially enhancing qubit performance in terms of junction parameter variation, stability, and controllability, though not necessarily improving coherence times significantly. This approach for improving the JJ region contrasts the desired path for minimizing loss by reducing grain boundaries in superconducting coplanar waveguide resonators using Nb film circuit layers [74].

4. Conclusions

In summary, we reveal that the deposition rate of Al film does not significantly impact qubit's coherence time, despite obvious differences in barrier oxide morphology and thickness variation. Samples fabricated with higher Al deposition rates exhibit a more uniform and less wavy Al-oxide layer. Other factors, such as grain sizes, surface roughness, grain boundary grooving, and hillock formation of Al layers, influence the spatial variation of the AlO_x barrier and contribute to junction failures as well. Additionally, we observe electronic structure variations across the AlO_x barrier, with the average Al coordination number being higher closer to the upper Al/AlO_x interface. This inhomogeneity indicates the presence of point defects in the AlO_x layer, which may act as dissipation sources in the superconducting qubits. Furthermore, we directly observe stress-induced GBS that leads to short-circuit failure in JJ. Our comprehensive study on JJ microstructure as a function of deposition rate provides guidance for future improvements in JJ microstructure.

CRediT authorship contribution statement

Jin-Su Oh: Data curation, Formal analysis, Investigation, Writing – original draft, Writing – review & editing. **Cameron J. Kopas:** Data curation, Formal analysis, Investigation, Writing – review & editing, Conceptualization, Project administration, Writing – original draft. **Hilal Cansizoglu:** Data curation, Writing – review & editing. **Joshua Y. Mutus:** Writing – review & editing. **Kameshwar Yadavalli:** Writing – review & editing. **Tae-Hoon Kim:** Data curation. **Matt Kramer:** Funding acquisition, Project administration, Writing – review & editing. **Alexander H. King:** Writing – review & editing, Investigation. **Lin Zhou:** Conceptualization, Formal analysis, Funding acquisition, Investigation, Project administration, Supervision, Writing – original draft, Writing – review & editing.

Declaration of competing interest

The authors declare that they have no known competing financial interests or personal relationships that could have appeared to influence the work reported in this paper.

Acknowledgments

This work was supported by the U.S. Department of Energy, Office of

Science, National Quantum Information Science Research Centers, Superconducting Quantum Materials and Systems Center (SQMS) under contract No. DE-AC02–07CH11359. All electron microscopy and related work were performed using instruments in the Sensitive Instrument Facility in Ames Lab. The Ames Laboratory is operated for the U.S. Department of Energy by Iowa State University under Contract No. DE-AC02–07CH11358. We thank Rigetti fab team members for the process development and fabrication of studied specimens.

References

[1] M.H. Devoret, R.J. Schoelkopf, Superconducting circuits for quantum information: an outlook, Science 339 (1979) 1169–1174, https://doi.org/10.1126/science.1231930 (1979)2013.
[2] J.M. Martinis, M.H. Devoret, J. Clarke, Quantum Josephson junction circuits and the dawn of artificial atoms, Nat. Phys. 16 (2020) 234–237, https://doi.org/10.1038/s41567-020-0829-5.
[3] T.P. Orlando, J.E. Mooij, L. Tian, C.H. Van Der Wal, L.S. Levitov, S. Lloyd, J. J. Mazo, Superconducting persistent-current qubit, Phys. Rev. B Condens. Matter Mater. Phys. 60 (1999) 15398–15413, https://doi.org/10.1103/PhysRevB.60.15398.
[4] Y. Nakamura, Y. ~A. Pashkin, J. ~S. Tsai, Coherent control of macroscopic quantum states in a single-Cooper-pair box, Nature 398 (1999) 786–788.
[5] J. Clarke, F.K. Wilhelm, Superconducting quantum bits, Nature 453 (2008) 1031–1042, https://doi.org/10.1038/nature07128.
[6] J.Q. You, F. Nori, Atomic physics and quantum optics using superconducting circuits, Nature 474 (2011) 589–597, https://doi.org/10.1038/nature10122.
[7] M. Kjaergaard, M.E. Schwartz, J. Braumüller, P. Krantz, J.I.J. Wang, S. Gustavsson, W.D. Oliver, Superconducting Qubits: current state of play, Annu Rev. Condens. Matter Phys. 11 (2020) 369–395, https://doi.org/10.1146/annurev-conmatphys-031119-050605.
[8] W.D. Oliver, P.B. Welander, Materials in superconducting quantum bits, MRS Bull. 38 (2013) 816–825, https://doi.org/10.1557/mrs.2013.229.
[9] N.P. de Leon, K.M. Itoh, D. Kim, K.K. Mehta, T.E. Northup, H. Paik, B.S. Palmer, N. Samarth, S. Sangtawesin, D.W. Steuerman, Materials challenges and opportunities for quantum computing hardware, Science (1979) 372, https://doi.org/10.1126/science.abb2823 (1979)2021.
[10] J. Lisenfeld, G.J. Grabovskij, C. Müller, J.H. Cole, G. Weiss, A.V. Ustinov, Observation of directly interacting coherent two-level systems in an amorphous material, Nat. Commun. 6 (2015) 1–6, https://doi.org/10.1038/ncomms7182.
[11] J.M. Gambetta, J.M. Chow, M. Steffen, Building logical qubits in a superconducting quantum computing system, npj Quantum Inf. 3 (2017) 2, https://doi.org/10.1038/s41534-016-0004-0.
[12] L.J. Zeng, S. Nik, T. Greibe, P. Krantz, C.M. Wilson, P. Delsing, E. Olsson, Direct observation of the thickness distribution of ultra thin AlOx barriers in Al/AlOx/Al Josephson junctions, J. Phys. D Appl. Phys. 48 (2015) 395308, https://doi.org/10.1088/0022-3727/48/39/395308.
[13] T. Aref, A. Averin, S. Van Dijken, A. Ferring, M. Koberidze, V.F. Maisi, H. Q. Nguyend, R.M. Nieminen, J.P. Pekola, L.D. Yao, Characterization of aluminum oxide tunnel barriers by combining transport measurements and transmission electron microscopy imaging, J. Appl. Phys. 116 (2014), https://doi.org/10.1063/1.4893473.
[14] S. Fritz, L. Radtke, R. Schneider, M. Weides, D. Gerthsen, Optimization of Al/AlOx/Al-layer systems for Josephson junctions from a microstructure point of view, J. Appl. Phys. 125 (2019) 165301, https://doi.org/10.1063/1.5089871.
[15] S. Nik, P. Krantz, L. Zeng, T. Greibe, H. Pettersson, S. Gustafsson, P. Delsing, E. Olsson, Correlation between Al grain size, grain boundary grooves and local variations in oxide barrier thickness of Al/AlOx/Al tunnel junctions by transmission electron microscopy, Springerplus 5 (2016), https://doi.org/10.1186/s40064-016-2418-8.
[16] L. Zeng, D.T. Tran, C.W. Tai, G. Svensson, E. Olsson, Atomic structure and oxygen deficiency of the ultrathin aluminium oxide barrier in Al/AlOx/Al Josephson junctions, Sci. Rep. 6 (2016) 1–8, https://doi.org/10.1038/srep29679.
[17] S. Fritz, A. Seiler, L. Radtke, R. Schneider, M. Weides, G. Weiß, D. Gerthsen, Correlating the nanostructure of Al-oxide with deposition conditions and dielectric contributions of two-level systems in perspective of superconducting quantum circuits, Sci. Rep. 8 (2018) 1–12, https://doi.org/10.1038/s41598-018-26066-4.
[18] S. Fritz, L. Radtke, R. Schneider, M. Luysberg, M. Weides, D. Gerthsen, Structural and nanochemical properties of Al Ox layers in Al/Al Ox/Al -layer systems for Josephson junctions, Phys. Rev. Mater. 3 (2019) 1–11, https://doi.org/10.1103/PhysRevMaterials.3.114805.
[19] M. Gurvitch, M.A. Washington, H.A. Huggins, High quality refractory Josephson tunnel junctions utilizing thin aluminum layers, Appl. Phys. Lett. 42 (1983) 472–474, https://doi.org/10.1063/1.93974.
[20] C.T. Rogers, R.A. Bunhrman, Nature of single-localized-electron states derived from tunneling measurements, 1985.
[21] R.T. Wakai, D.J. Van Harlingen, Low-frequency noise and discrete charge trapping in small-area tunnel junction dc SQUID's, Appl. Phys. Lett. 49 (1986) 593–595, https://doi.org/10.1063/1.97051.
[22] C. Müller, J.H. Cole, J. Lisenfeld, Towards understanding two-level-systems in amorphous solids: insights from quantum circuits, Rep. Prog. Phys. 82 (2019) 124501, https://doi.org/10.1088/1361-6633/ab3a7e.
[23] T.C. Dubois, M.C. Per, S.P. Russo, J.H. Cole, Delocalized oxygen as the origin of two-level defects in josephson junctions, Phys. Rev. Lett. 110 (2013) 1–5, https://doi.org/10.1103/PhysRevLett.110.077002.
[24] P. Dutta, P.M. Horn, Low-frequency fluctuations in solids: 1/f noise, Rev. Mod. Phys. 53 (1981) 497–516, https://doi.org/10.1103/RevModPhys.53.497.
[25] A. Shnirman, G. Schön, I. Martin, Y. Makhlin, Low- And high-frequency noise from coherent two-level systems, Phys. Rev. Lett. 94 (2005) 1–4, https://doi.org/10.1103/PhysRevLett.94.127002.
[26] J. Burnett, L. Faoro, I. Wisby, V.L. Gurtovoi, A.V. Chernykh, G.M. Mikhailov, V. A. Tulin, R. Shaikhaidarov, V. Antonov, P.J. Meeson, A.Y. Tzalenchuk, T. Lindström, Evidence for interacting two-level systems from the 1/f noise of a superconducting resonator, Nat. Commun. 5 (2014) 1–6, https://doi.org/10.1038/ncomms5119.
[27] R. McDermott, Materials origins of decoherence in superconducting qubits, IEEE Trans. Appl. Supercond. 19 (2009) 2–13, https://doi.org/10.1109/TASC.2008.2012255.
[28] M.S. Alam, S. Belomestnykh, N. Bornman, G. Cancelo, Y.-C. Chao, M. Checchin, V. S. Dinh, A. Grassellino, E.J. Gustafson, R. Harnik, C.R.H. McRae, Z. Huang, K. Kapoor, T. Kim, J.B. Kowalkowski, M.J. Kramer, Y. Krasnikova, P. Kumar, D.M. Kurkcuoglu, H. Lamm, A.L. Lyon, D. Milathianaki, A. Murthy, J. Mutus, I. Nekrashevich, J. Oh, A.B. Özgüler, G.N. Perdue, M. Reagor, A. Romanenko, J.A. Sauls, L. Stefanazzi, D. Venturelli, C. Wang, X. You, D.M.T. van Zanten, L. Zhou, S. Zhu, S. Zorzetti, Quantum computing hardware for HEP algorithms and sensing, (2022) 1–23.
[29] M. Bal, A.A. Murthy, S. Zhu, F. Crisa, X. You, Z. Huang, T. Roy, J. Lee, D. van Zanten, R. Pilipenko, I. Nekrashevich, A. Lunin, D. Bafia, Y. Krasnikova, C.J. Kopas, E.O. Lachman, D. Miller, J.Y. Mutus, M.J. Reagor, H. Cansizoglu, J. Marshall, D. P. Pappas, K. Vu, K. Yadavalli, J.-S. Oh, L. Zhou, M.J. Kramer, F.Q. Lecocq, D. P. Goronzy, C.G. Torres-Castanedo, G. Pritchard, V.P. Dravid, J.M. Rondinelli, M. J. Bedzyk, M.C. Hersam, J. Zasadzinski, J. Koch, J.A. Sauls, A. Romanenko, A. Grassellino, Systematic improvements in transmon qubit coherence enabled by niobium surface encapsulation, npj Quantum Inf. 10 (2024) 43, https://doi.org/10.1038/s41534-024-00840-x.
[30] J.S. Oh, R. Zaman, A.A. Murthy, M. Bal, F. Crisa, S. Zhu, C.G. Torres-Castendo, C. J. Kopas, J.Y. Mutus, D. Jing, J. Zasadzinski, A. Grassellino, A. Romanenko, M. C. Hersam, M.J. Bedzyk, M. Kramer, B.C. Zhou, L. Zhou, Structure and formation mechanisms in tantalum and niobium oxides in superconducting quantum circuits, ACS Nano 18 (2024) 19732–19741, https://doi.org/10.1021/acsnano.4c05251.
[31] M. Constantin, C.C. Yu, Microscopic model of critical current noise in Josephson junctions, Phys. Rev. Lett. 99 (2007), https://doi.org/10.1103/PhysRevLett.99.207001.
[32] C.D. Nugroho, V. Orlyanchik, D.J. Van Harlingen, Low frequency resistance and critical current fluctuations in Al-based Josephson junctions, Appl. Phys. Lett. 102 (2013), https://doi.org/10.1063/1.4801521.
[33] D.J. Van Harlingen, T.L. Robertson, B.L.T. Plourde, P.A. Reichardt, T.A. Crane, J. Clarke, Decoherence in Josephson-junction qubits due to critical-current fluctuations, Phys. Rev. B Condens. Matter Mater. Phys. 70 (2004), https://doi.org/10.1103/PhysRevB.70.064517.
[34] D. Willsch, D. Rieger, P. Winkel, M. Willsch, C. Dickel, J. Krause, Y. Ando, R. Lescanne, Z. Leghtas, N.T. Bronn, P. Deb, O. Lanes, Z.K. Minev, B. Dennig, S. Geisert, S. Günzler, S. Ihssen, P. Paluch, T. Reisinger, R. Hanna, J.H. Bae, P. Schüffelgen, D. Grützmacher, L. Buimaga-Iarinca, C. Morari, W. Wernsdorfer, D. P. DiVincenzo, K. Michielsen, G. Catelani, I.M. Pop, Observation of Josephson harmonics in tunnel junctions, Nat. Phys. 20 (2024) 815–821, https://doi.org/10.1038/s41567-024-02400-8.
[35] W. Oepts, H.J. Verhagen, R. Coehoorn, W.J.M. De Jonge, Analysis of breakdown in ferromagnetic tunnel junctions, J. Appl. Phys. 86 (1999) 3863–3872, https://doi.org/10.1063/1.371300.
[36] N.P. Magtoto, C. Niu, B.M. Ekstrom, S. Addepalli, J.A. Kelber, Dielectric breakdown of ultrathin aluminum oxide films induced by scanning tunneling microscopy, Appl. Phys. Lett. 77 (2000) 2228–2230, https://doi.org/10.1063/1.1313816.
[37] N.P. Magtoto, C. Niu, M. Anzaldua, J.A. Kelber, D.R. Jennison, STM-induced void formation at the Al2O3/Ni3Al(1 1 1) interface, Surf. Sci. 472 (2001) L157–L163, https://doi.org/10.1016/S0039-6028(00)00948-1.
[38] S.K. Tolpygo, D. Amparo, Electrical stress effect on Josephson tunneling through ultrathin AlOx barrier in Nb/Al/AlOx /Nb junctions, J. Appl. Phys. 104 (2008), https://doi.org/10.1063/1.2977725.
[39] P. Tyagi, B.J. Hinds, Mechanism of ultrathin tunnel barrier failure due to mechanical-stress-induced nanosized hillocks and voids, J. Vac. Sci. Technol. B 28 (2010) 517–521, https://doi.org/10.1116/1.3406143. Nanotechnology and Microelectronics: Materials, Processing, Measurement, and Phenomena.
[40] K. Bayros, M.J. Cyster, J.S. Smith, J.H. Cole, Influence of pinholes and weak-points in aluminum-oxide Josephson junctions, Phys. Rev. Mater. 8 (2024), https://doi.org/10.1103/PhysRevMaterials.8.046202.
[41] A. Nersisyan, E.A. Sete, S. Stanwyck, A. Bestwick, M. Reagor, S. Poletto, N. Alidoust, R. Manenti, R. Renzas, C.V. Bui, K. Vu, T. Whyland, Y. Mohan, Manufacturing low dissipation superconducting quantum processors, in: Proceedings of the Technical Digest - International Electron Devices Meeting, IEDM 2019-Decem, 2019, https://doi.org/10.1109/IEDM19573.2019.8993458.
[42] W.W. Mullins, The effect of thermal grooving on grain boundary motion, Acta Metall. 6 (1958) 414–427, https://doi.org/10.1016/0001-6160(58)90020-8.
[43] H.P. Longworth, C.V. Thompson, Abnormal grain growth in aluminum alloy thin films, J. Appl. Phys. 69 (1991) 3929–3940, https://doi.org/10.1063/1.348452.

[44] M.M. Nowell, D.P. Field, Texture and grain boundary structure dependence of hillock formation in thin metal films, Mater. Res. Soc. Symp. Proc. 516 (1998) 115–120, https://doi.org/10.1557/proc-516-115.
[45] C.V. Thompson, Grain growth in thin films, Annu. Rev. Mater. Sci. 20 (1990) 245–268, https://doi.org/10.1146/annurev.ms.20.080190.001333.
[46] C.V. Thompson, R. Carel, Stress and grain growth in thin films, J. Mech. Phys. Solids 44 (1996) 657–673, https://doi.org/10.1016/0022-5096(96)00022-1.
[47] H.J. Frost, C.V. Thompson, D.T. Walton, Simulation of thin film grain structures-II. Abnormal grain growth, Acta Metall. Mater. 40 (1992) 779–793, https://doi.org/10.1016/0956-7151(92)90020-F.
[48] C. Weigel, G. Calas, L. Cormier, L. Galoisy, G.S. Henderson, High-resolution Al L2,3-edge x-ray absorption near edge structure spectra of Al-containing crystals and glasses: coordination number and bonding information from edge components, J. Phys. Condens. Matter 20 (2008), https://doi.org/10.1088/0953-8984/20/13/135219.
[49] D. Bouchet, C. Colliex, Experimental study of ELNES at grain boundaries in alumina: intergranular radiation damage effects on Al-L23 and O-K edges, Ultramicroscopy 96 (2003) 139–152, https://doi.org/10.1016/S0304-3991(02)00437-0.
[50] K. Kimoto, Y. Matsui, T. Nabatame, T. Yasuda, T. Mizoguchi, I. Tanaka, A. Toriumi, Coordination and interface analysis of atomic-layer-deposition Al2O3 on Si(001) using energy-loss near-edge structures, Appl. Phys. Lett. 83 (2003) 4306–4308, https://doi.org/10.1063/1.1629397.
[51] T.C. DuBois, M.J. Cyster, G. Opletal, S.P. Russo, J.H. Cole, Constructing ab initio models of ultra-thin Al-AlOx-Al barriers, Mol. Simul. 42 (2016) 542–548, https://doi.org/10.1080/08927022.2015.1068941.
[52] J. Gorobez, B. Maack, N. Nilius, Growth of self-passivating oxide layers on aluminum—pressure and temperature dependence, Phys. Status Solidi B Basic Res. 258 (2021), https://doi.org/10.1002/pssb.202000559.
[53] H. Jung, Y. Kim, K. Jung, H. Im, Y.A. Pashkin, O. Astafiev, Y. Nakamura, H. Lee, Y. Miyamoto, J.S. Tsai, Potential barrier modification and interface states formation in metal-oxide-metal tunnel junctions, Phys. Rev. B 80 (2009) 3–8, https://doi.org/10.1103/PhysRevB.80.125413.
[54] D.P. Pappas, M. Field, C.J. Kopas, J.A. Howard, X. Wang, E. Lachman, J. Oh, L. Zhou, A. Gold, G.M. Stiehl, K. Yadavalli, E.A. Sete, A. Bestwick, M.J. Kramer, J. Y. Mutus, Alternating-bias assisted annealing of amorphous oxide tunnel junctions, Commun. Mater. 5 (2024) 150, https://doi.org/10.1038/s43246-024-00596-z.
[55] M. Hershkovitz, I.A. Blech, Y. Komem, Stress relaxation in thin aluminium films, Thin Solid Films 130 (1985) 87–93, https://doi.org/10.1016/0040-6090(85)90298-6.
[56] R.C. Cammarata, T.M. Trimble, Surface stress model for intrinsic stresses in thin films, J. Mater. Res. 15 (2000) 2468–2474.
[57] R. Koch, Stress in evaporated and sputtered thin films – a comparison, Surf. Coat. Technol. 204 (2010) 1973–1982, https://doi.org/10.1016/j.surfcoat.2009.09.047.
[58] J. Kohout, E. Bousser, T. Schmitt, R. Vernhes, O. Zabeida, J. Klemberg-Sapieha, L. Martinu, Stable reactive deposition of amorphous Al2O3 films with low residual stress and enhanced toughness using pulsed dc magnetron sputtering with very low duty cycle, Vacuum 124 (2016) 96–100, https://doi.org/10.1016/j.vacuum.2015.11.017.
[59] K. Owusu-Boahen, A.H. King, Early stages of plastic yielding in polycrystalline gold thin films, Acta Mater. 49 (2001) 237–247, https://doi.org/10.1016/S1359-6454(00)00315-3.
[60] H. Van Swygenhoven, M. Spaczer, A. Caro, Microscopic description of plasticity in computer generated metallic nanophase samples: a comparison between Cu and Ni, Acta Mater. 47 (1999) 3117–3126, https://doi.org/10.1016/S1359-6454(99)00109-3.
[61] H. Conrad, J. Narayan, On the grain size softening in nanocrystalline materials, Scr. Mater. 42 (2000) 1025–1030, https://doi.org/10.1016/S1359-6462(00)00320-1.
[62] K. Maung, J.C. Earthman, F.A. Mohamed, Inverse Hall-Petch behavior in diamantane stabilized bulk nanocrystalline aluminum, Acta Mater. 60 (2012) 5850–5857, https://doi.org/10.1016/j.actamat.2012.07.026.
[63] T.G. Langdon, Grain boundary sliding revisited: developments in sliding over four decades, J. Mater. Sci. 41 (2006) 597–609, https://doi.org/10.1007/s10853-006-6476-0.
[64] R.C. Gifkins, A. Gittins, R.L. Bell, T.G. Langdon, The dependence of grain-boundary sliding on shear stress, J. Mater. Sci. 3 (1968) 306–313, https://doi.org/10.1007/BF00741967.
[65] M.A. Linne, T.R. Bieler, S. Daly, The effect of microstructure on the relationship between grain boundary sliding and slip transmission in high purity aluminum, Int. J. Plast. 135 (2020) 102818, https://doi.org/10.1016/j.ijplas.2020.102818.
[66] M.Y. Gutkin, I.A. Ovid'ko, N.V. Skiba, Crossover from grain boundary sliding to rotational deformation in nanocrystalline materials, Acta Mater. 51 (2003) 4059–4071, https://doi.org/10.1016/S1359-6454(03)00226-X.
[67] G.S. Rohrer, X. Liu, J. Liu, A. Darbal, M.N. Kelly, X. Chen, M.A. Berkson, N. T. Nuhfer, K.R. Coffey, K. Barmak, The grain boundary character distribution of highly twinned nanocrystalline thin film aluminum compared to bulk microcrystalline aluminum, J. Mater. Sci. 52 (2017) 9819–9833, https://doi.org/10.1007/s10853-017-1112-8.
[68] A. Venkataraman, M. Linne, S. Daly, M.D. Sangid, Criteria for the prevalence of grain boundary sliding as a deformation mechanism, Materialia 8 (2019) 100499, https://doi.org/10.1016/j.mtla.2019.100499 (Oxf).
[69] A. Venkataraman, M.D. Sangid, A crystal plasticity model with an atomistically informed description of grain boundary sliding for improved predictions of deformation fields, Comput. Mater. Sci. 197 (2021) 110589, https://doi.org/10.1016/j.commatsci.2021.110589.
[70] R.H.J. Kim, J.M. Park, S. Haeuser, C. Huang, D. Cheng, T. Koschny, J. Oh, C. Kopas, H. Cansizoglu, K. Yadavalli, J. Mutus, L. Zhou, L. Luo, M.J. Kramer, J. Wang, Visualizing heterogeneous dipole fields by terahertz light coupling in individual nano-junctions, Commun. Phys. 6 (2023) 1–7, https://doi.org/10.1038/s42005-023-01259-0.
[71] V.A. Kotenev, Combining ellipsometry and electron microscopy for identifying the initial stages of aluminum oxidation. II. Ellipsometry, Prot. Met. 36 (2000) 409–418, https://doi.org/10.1007/BF02764085.
[72] B. Bonin, H. Safa, Power dissipation at high fields in granular RF superconductivity, Supercond. Sci. Technol. 4 (1991) 257–261, https://doi.org/10.1088/0953-2048/4/6/008.
[73] A. Premkumar, C. Weiland, S. Hwang, B. Jäck, A.P.M. Place, I. Waluyo, A. Hunt, V. Bisogni, J. Pelliciari, A. Barbour, M.S. Miller, P. Russo, F. Camino, K. Kisslinger, X. Tong, M.S. Hybertsen, A.A. Houck, I. Jarrige, Microscopic relaxation channels in materials for superconducting qubits, Commun. Mater. 2 (2021) 72, https://doi.org/10.1038/s43246-021-00174-7.
[74] J.S. Oh, C.J. Kopas, J. Marshall, X. Fang, K.R. Joshi, A. Datta, S. Ghimire, J.M. Park, R. Kim, D. Setiawan, E. Lachman, J.Y. Mutus, A.A. Murthy, A. Grassellino, A. Romanenko, J. Zasadzinski, J. Wang, R. Prozorov, K. Yadavalli, M. Kramer, L. Zhou, Exploring the relationship between deposition method, microstructure, and performance of Nb/Si-based superconducting coplanar waveguide resonators, Acta Mater. 276 (2024) 120153, https://doi.org/10.1016/j.actamat.2024.120153.